Origin of surface and subband states at the InAs(111)A surface

Rajib Batabyal,* Steffen Zelzer, and Alec P. Romagosa
Center for Quantum Devices, Niels Bohr Institute, University of Copenhagen, 2100 Copenhagen, Denmark

Derek Dardzinski
Department of Materials Science and Engineering, Carnegie Mellon University, Pittsburgh, Pennsylvania 15213, USA

Fabiano Corsetti
Microsoft Quantum Materials Lab Copenhagen, 2800 Lyngby, Denmark

Noa Marom
Department of Materials Science and Engineering, Carnegie Mellon University, Pittsburgh, Pennsylvania 15213, USA;
Department of Physics, Carnegie Mellon University, Pittsburgh, Pennsylvania 15213, USA;
and Department of Chemistry, Carnegie Mellon University, Pittsburgh, Pennsylvania 15213, USA

Peter Krogstrup†
NNF Quantum Computing Programme, Niels Bohr Institute, University of Copenhagen, 2100 Copenhagen, Denmark

(Received 17 January 2023; revised 16 May 2023; accepted 23 May 2023; published 20 June 2023)

The atomic structure of surfaces and interfaces plays a vital role in the electronic quality and properties of quantum devices. The interplay between the surface and confined bulk subband states in terms of their susceptibility has been investigated in relation to crystal defects on an InAs(111)A-(2 × 2) reconstructed surface, using low-temperature scanning tunneling microscopy and spectroscopy. We measure the two-dimensional quantized subband states arising from the confined potential imposed by downward bending of the conduction band edge. Furthermore, we show evidence of the existence of surface Bloch states within the confined bulk band gap projected on the surface spectrum which have originated from the surface reconstruction. As expected, larger confined bulk band gaps at the surface and conduction band offset are measured to be 0.58 and 0.31 eV, respectively. We further show the scattering of these quantum states at different surface defects and demonstrate that surface states are more susceptible to the defect potential when compared with the corresponding subband states. This apparent contrast follows from the length scale at which these defect potentials actively interact on or near the surface. Our observed experimental results are supported by empirical tight-binding simulations for the subband states and first-principles density functional theory simulations for the surface states present on the surface.

DOI: 10.1103/PhysRevMaterials.7.066201

I. INTRODUCTION

Compound semiconductors have become indispensable, not only as thin-film heterostructure elements, but also as a nanotechnology material. InAs is a III-V compound semiconductor with high mobility, a narrow direct band gap [1], and large spin-orbit interaction [2]. These properties qualify InAs as a good candidate for high-speed devices [3], far-infrared photonic devices [4], and spintronics applications [5]. InAs proximitized by the superconductor Al is one of the most promising material platforms for the realization of topologically protected quantum bits based on Majorana fermions [6,7].

In As(111)A is often employed as a reliable model platform for investigations of many-body interactions underlying this technology and other quantum technologies [8] due to its electron accumulation layer, hosting a two-dimensional (nearly) free electron gas (2DEG). Furthermore, InAs(111)A has previously been shown to offer a platform for scanning-probe-based nanostructure assembly [9]. However, the origin of the charge accumulation layer on the InAs(111)A surface is still under debate. At present, it is believed that the Fermi level is pinned just below the conduction band minimum (CBM) due to native indium adatoms In_{ad} and indium antisite In_{As} impurities, appearing above and below the In-vacancy sites of the stable 2 × 2 reconstruction, forming ionic-like bonds and hence acting as a single-electron donor to the conduction band (CB) [10,11]. This would pose a fundamentally different mechanism of Fermi level pinning compared with the InAs(001) surface, where dangling bonds of the surface reconstruction have been identified as the origin of band bending.

*Present address: UGC-DAE Consortium for Scientific Research, Indore, India; rajibbatabyal@gmail.com
†krogstrup@nbi.ku.dk

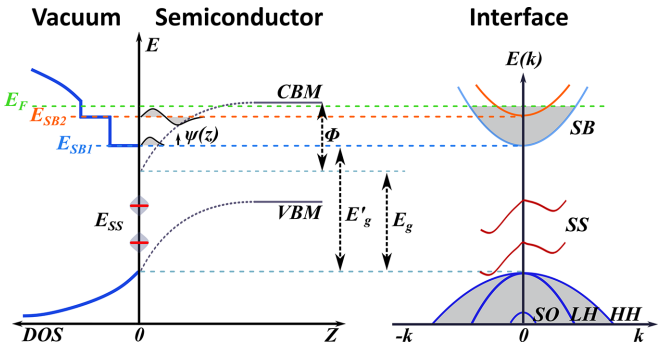

FIG. 1. Schematic band diagram of the vacuum-InAs interface showing the downwards band bending at the surface. The Fermi energy is located slightly below the bulk CBM. Near the surface, the bending of the conduction band below the Fermi level creates a 2D quantum well resulting in the subband states (SB; E_{SB1} and E_{SB2}). Energy positions of surface states (SS; E_{SS}) are shown in the band gap at the surface. The lowest subband energy and the VBM represent the apparent band gap E_g' at the surface, which is larger than the bulk band gap E_g. Φ represents the conduction band offset.

On both the surfaces, the carrier density is comparable and on the order of 1–4 $\times$ 10^{12} cm^{-2} [12,13]. The origin of the *p*-type surface that is responsible for the charge accumulation may be affected by other contributions besides the surface structure, such as adatoms or structural defects. With simulations we show that dangling bonds produce gap states but do not shift the band edge positions, while O being adsorbed does affect the band bending [14].

The concept of downwards band bending due to Fermi level pinning and formation of subband states is shown schematically in Fig. 1. In the left panel, the band diagram in real space, in which the CBM and valence band maximum (VBM) bend downward when approaching the surface, is shown. The electron accumulation layer extends deep into the crystal (∼23 nm) compared with the depth of the surface reconstruction [0.54 nm or ∼1.5 atomic layers (ALs)] [8]. The Fermi energy of the system is pinned just below the CB. The two-dimensional (2D) quantized subbands of the accumulated electrons with the energies E_{SB1} and E_{SB2} are part of the bulk conduction band, and their 2D densities of states (DOSs) appear as a step-function-like feature. Additionally, the surface reconstruction may lead to surface states in the band gap at the surface as marked exemplarily by E_{SS}: E_{SS1} and E_{SS2}. These states are localized to the top one to two ALs of the surface and decay exponentially into the bulk and vacuum.

In the right panel, we show the schematic surface band structure of InAs in reciprocal space, where the energy gap E_g' between the lowest subband and onset energy of the VBM defines the confined energy band gap that projects on the surface, below the Fermi energy, with a value larger than the bulk energy gap E_g. This apparent increase in surface projected band gap arises due to the quantization of the conduction band near the surface. In the valence band, heavy-hole (HH), light-hole (LH), and split-off (SO) bands arise due to the strong spin-orbit coupling in InAs (energy not to scale). The conduction band offset Φ is defined by the energy offset of the bulk CBM due to the band bending on the surface.

In this paper, we visualize the subband states and surface states within the projected energy gap below the Fermi energy and estimate this energy gap projected on the surface using low-temperature scanning tunneling microscopy (LT-STM) and spectroscopy (LT-STS) techniques on the clean InAs(111)A-(2 × 2) surface. Combining experimentally extracted subband locations with tight-binding simulation data, the conduction band offset is estimated in Sec. III A. We then trace the origin of surface states back to the reconstruction by comparing the experimentally observed surface states with density functional theory simulations in Sec. III B. We discuss their local structure and address the fact that these surface states are mostly emerging from As atoms. Finally, in Sec. III C, we investigate the interaction of the surface states and the subband states with the defect potential of a step edge. We find that the surface states are strongly perturbed compared with the subband states and argue that this follows from the relative length scale at which the defect potential interacts with the electronic states.

II. METHODS

A. Sample preparation and experimental setup

Epitaxial growth was carried out on a quarter of a 2-in. epi-ready InAs(111)A wafer (miscut ±0.1°, undoped, *n*-type; Wafer Technology) in a molecular beam epitaxy (MBE) system (OCTOPLUS 600; Dr. Eberl MBE-Komponenten) using all solid sources. A valved cracker cell was used for arsenic (As), and a double-filament effusion cell was used for indium (In). After an initial degassing at 200 °C for 10 h upon introduction to the cluster, the native oxide was removed by atomic hydrogen cleaning at a sample temperature of 250 °C and a hydrogen pressure of 2.5 × 10^{-5} mbar for 10 min. Afterwards, 50 nm of InAs buffer were grown at a growth rate of 0.1 monolayers (MLs) per second, an As_2/In effective flux ratio of 30, and a sample temperature of 490 °C. After the buffer growth, the sample was cooled to 250 °C and capped with 30 nm of amorphous arsenic. The sample was unloaded and stored in a nitrogen cabinet for later use. An about 10 × 10 mm^2 piece of it was glued with pure gallium onto an Omicron-style tantalum flag holder. After the same degassing procedure (10 h, 200 °C) for introducing the sample to ultra-high vacuum (UHV) again, the As capping layer was removed by annealing the sample to around 250–300 °C for 4 h in vacuum, followed by further degassing it at 200 °C for 2 h. This procedure recovered the MBE-grown InAs(111)A-(2 × 2) reconstructed surface as detected by STM measurements after UHV *in situ* transfer to the STM (LT Nanoprobe 4P; Scienta Omicron).

All STM measurements presented here were performed using liquid helium cooling, resulting in a sample temperature of 4.3 K. Commercially available, electrochemically etched tungsten tips (Scienta Omicron) were employed, and typical topography scan parameters consisted of $V_g = 2.5$ V, $I_T = 70$ pA. Differential conductance spectra were recorded utilizing a lock-in amplifier for multiple locations along a line, averaging over ∼100 repetitions in each location. The sample drift during recording of the spectra was measured to be negligible. The energy resolution is 12.5 meV, considering

the sample temperature and the employed lock-in ac bias voltage of $V_{p\text{-}p} = 10$ meV with different modulation frequencies ranging from 700 to 900 Hz.

B. Computational details

To describe the system, and theoretically predict the features of interest, we employ atomistic modeling of the crystal surface and bulk. We make use of two distinct models, each appropriate for describing different features. The subband states require an accurate description of the long-range electrostatic potential decay into the bulk of the crystal in the range ∼10–100 nm, for which we use an empirical tight-binding (TB) methodology; in contrast, the surface states require an atomically accurate description of the details of the surface reconstruction and non-bulk-like bonding chemistry, for which we use a first-principles density functional theory (DFT) methodology.

TB calculations were performed using the QUANTUMATK code [15], version T-2022.03. The Slater-Koster orthogonal model with InAs parametrization from Jancu *et al.* [16] was used, including spin-orbit coupling. For bulk InAs, the model gives a band gap of 0.418 eV, spin-orbit splitting of 0.38 eV, and conduction band effective mass of 0.024, in good agreement with experimental values (0.417 eV, 0.39 eV, and 0.026, respectively [17].)

The system was modeled as a slab of 186 layers (∼33 nm) of InAs(111), with unreconstructed surfaces and hydrogen termination in order to remove any unphysical surface states. The long-range band bending profile (slowly varying on the length scale of atomic layers) is included as an additional on-site potential, calculated self-consistently by imposing a fixed band offset at one surface as a boundary condition to the Poisson equation.

DFT calculations were performed using the Vienna *ab initio* simulation package (VASP) code [18–22] with the projector-augmented wave (PAW) method [18,23]. The generalized gradient approximation (GGA) of Perdew, Burke, and Ernzerhof (PBE) [24] was used to describe the exchange-correlation interactions between electrons. A Hubbard U correction within Dudarev's formalism [25] was applied to the p orbitals of both In and As. U_{eff} values were determined using a Bayesian optimization method [26] and were found to be -0.5 and -7.5 eV for In and As, respectively. These values have been used successfully for simulations of InAs surfaces and interfaces [26–28]. For all calculations, dipole corrections were applied along the z axis. Spin-orbit coupling was used throughout.

To generate the surface reconstruction, a 2×2 In-terminated InAs(111) surface was generated with 40 Å of vacuum using an InAs lattice parameter of 6.4794 Å. A single In atom was then removed from the top surface, and pseudo-hydrogen atoms with charges of $0.75e^-$ were appended to the bottom surface to passivate the dangling bonds that result from cleaving of the surface [29]. Next, relaxation of the top four atomic layers and the pseudo-hydrogen positions was performed until the Hellmann-Feynman forces acting on ions were below 0.01 eV/Å. During relaxation the As atoms in the second atomic layer moved to 0.09 Å below the top In atoms, putting them on approximately the same plane [30]. A similar procedure was followed to generate and relax the surface structure for models with an In vacancy as well as the unreconstructed slab, with relaxed pseudo-hydrogen atoms on both ends of the surface. For the In-vacancy surface we noticed that the As atoms moved closer to each other to form what appears to be an As dimer.

For all self-consistent field (SCF) and density of states (DOS) calculations, Γ-centered Monkhorst-Pack k-point grids of $5 \times 5 \times 1$ and $7 \times 7 \times 1$, respectively, were used. For band structure calculations, the surface Brillouin zone was projected onto a bulk k path along the K-Γ-K direction as described in Ref. [14]. Due to the quantum confinement effect, the band gap of semiconductor slab models depends on the number of layers. For the InAs(111)A-(2×2) surface model and the unreconstructed surface, 30 atomic layers were used. For the surface model with In-vacancy concentrations of 16.7%, 15 atomic layers were used, owing to the larger supercell size. With 30 and 15 atomic layers the band gap of InAs is 0.018 and 0.155 eV larger than the bulk band gap, respectively.

III. RESULTS AND DISCUSSION

A. Subband states and conduction band offset

We have performed scanning tunneling microscopy (STM) and spectroscopy (STS) on the InAs(111)A surface. A set of differential conductance spectra were taken in areas nearly free of surface defects which are proportional to the sample's local density of states (LDOS). By fitting a set of broadened step functions to the averaged STS data, we were able to extract the energy positions of the two subbands forming in the surface accumulation layer, representative of the clean surface DOS. Using these energy positions we found the band offset by comparison to TB calculations. These studies are summarized in Fig. 2. In Fig. 2(a) we present atomically resolved STM topography of the In-terminated InAs(111)A-(2×2) reconstructed surface. The inset shows a zoomed-in version with a relaxed stick-and-ball model of the surface unit cell overlaid. The surface contains native impurities such as single In adatoms, extra In vacancies, and step edges [10,31,32]. In Fig. 2(b), we present the spatial average STS spectrum as a function of sample bias voltage of a total of 1510 spectra, spread over 151 atomically clean locations, far from surface impurities [compare, e.g., the lower left area of Fig. 2(a)].

Just below the Fermi energy [33], we observe two 2D DOS features at $E_{\text{SB1}} = -143$ meV and $E_{\text{SB2}} = -52$ meV as marked by dashed blue and orange lines, respectively. Comparing the energy positions of these states in the band spectrum with the previously measured angle-resolved photoemission spectroscopy (ARPES) results on the InAs surface, we identify these states as the subbands forming in the surface accumulation layer [12,13]. We estimate the apparent band gap based on the projected energy gap on the surface to be $E_g' = 0.58 \pm 0.012$ eV by measuring the energy separation between the lowest subband position, $E_{\text{SB1}} = -0.143$ eV, and the valence band edge, approximately -0.73 eV [marked by a dashed line in Fig. 2(b)]. This value is larger compared with the bulk band gap ($E_g = 0.42$ eV) [8] of InAs as explained earlier in Fig. 1. The energy position of the valence band is

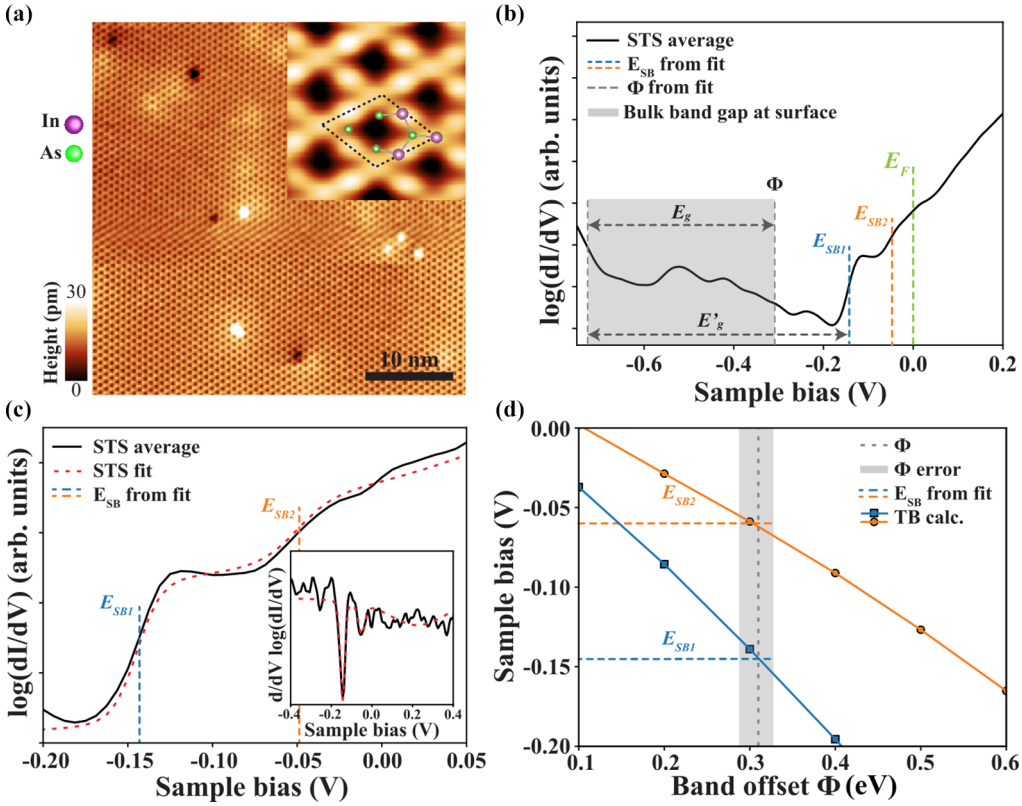

FIG. 2. Surface morphology and clean area spectroscopy. (a) Atomically resolved STM image ($V_g = 2.5$ V, $I_T = 70$ pA) of a clean area, exhibiting only a few native defects. The inset shows a zoomed-in view of the InAs(111)A-(2 × 2) reconstructed surface with a ball-and-stick model of the surface unit cell ($V_g = 2.5$ V, $I_T = 70$ pA). (b) Averaged spectrum (151 locations, ten repetitions) measured in a defect-free area. The 2D subband energy locations E_{SB1} and E_{SB2} as found from a step fit are marked. Surface state peaks are seen to appear in the bulk band gap at the surface (gray area). (c) Details of the fitting procedure to find the subband energies from the averaged spectra. The sum of three broadened step functions is fitted in the derivative space (red dashed line in inset). A good fit was achieved as indicated by the red dashed line following the averaged STS data closely. The subband energies are located at the inflection points of the fit. (d) The position of the first two subbands in the energy spectrum obtained from TB calculations with self-consistent electrostatics (filled rectangles and circles; see Appendix A for a more detailed visualization of the band structure) combined with the statistical results from applying the subband position fitting procedure to each of the 1510 spectra individually. The mean values of the first and second fitted subband energies independently cross the TB calculations at a band offset of $\Phi \sim 0.31$ eV.

extracted by analyzing the slope in the numerical derivative of the spectra where we find a sudden increase in the slope with a kink and employing the TB results that will be discussed later. The energy positions of the subbands were found by fitting a sum of three step functions to the derivative of the natural logarithm of the differential conductance data. The fit agrees well in this form and in normal logarithmic scales as shown in Fig. 2(c) and its inset. Applying this fitting to each single spectrum instead yielded a distribution of energy positions which is shown as E_{SB1} and E_{SB2} in Fig. 2(d) along with the subband energy as a function of conduction band offset from theoretical TB calculations of the surface accumulation layer. In Appendix A, Fig. 6, we show the calculated band structure from the TB model showing the subbands below the Fermi level. From the distribution, we found the median values for the subbands to be $E_{SB1} = -144$ meV and $E_{SB2} = -58$ meV, respectively. The histograms for both subbands are also shown in more detail in Appendix B, Fig. 7, from which we find that both the median and the energy positions extracted from the average STS data represent the data well. The intersection of the median of the distribution with these TB data is indicated by a vertical dashed line in Fig. 2(d) and independently leads to a band offset of $\Phi \approx -0.31$ eV for both subband energies. This gives us confidence in the accuracy of this value. Considering this value of band offset ($\Phi \approx -0.31$ eV) and along with the bulk band gap ($E_g = 0.42$ eV) of InAs, the valence band edge can be estimated to be approximately -0.73 eV (see Fig. 2), which is exactly the position where we get a kink in the numerical derivative of the spectra.

B. Origin of surface states

Apart from the subbands in the surface accumulation layer, we notice in Fig. 2(b) that the LDOS within the confined band gap is nonzero and shows well-defined quantum states at the energies -0.24, -0.34, -0.42, and -0.52 eV, respectively [marked by arrows in Fig. 3(d)]. Moreover, we found that the energy positions of these states change depending on the location. The appearance of such states has been previously observed and described in direct-band-gap III-V materials [34]. The bulk band gap of InAs does not host any states; this raises the question of the origin of these states. One

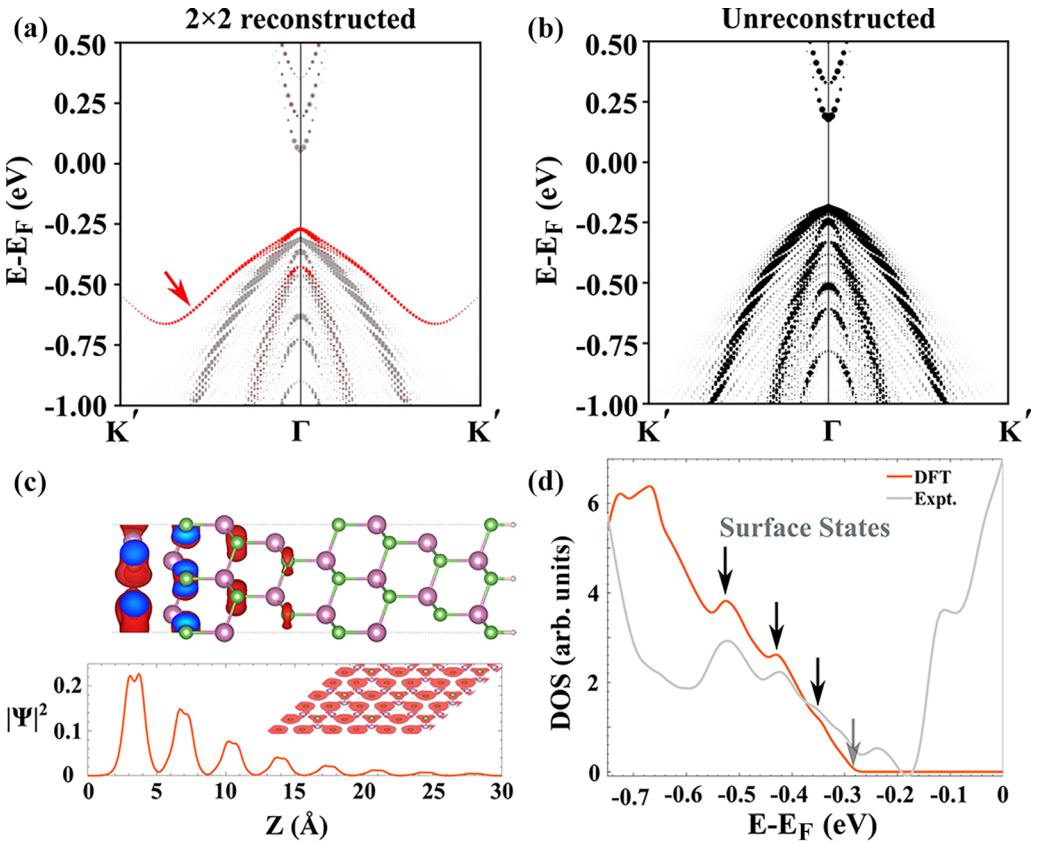

FIG. 3. Electronic band structure and the surface states' DOSs. (a) Calculated band structure of a 2 × 2 reconstructed InAs(111)A surface. The contributions of the top four atomic layers are colored in red. (b) Calculated band structure of an unreconstructed InAs(111)A surface. (c) Spatial localization of the surface states. (d) Comparison of the calculated electronic DOS with the experimental STS results. Black and gray arrows are the energy positions of the surface states; the gray arrow represents the onset energy of the first surface state in the simulated DOS below the band gap.

possible reason for their appearance could be the localized defect states due to native surface defects. However, these states are clearly resolved in spectroscopy measurements far from any crystal imperfections.

To elucidate the origin of the states in the band gap, we have performed DFT calculations. In Figs. 3(a) and 3(b) the calculated band structure of the only stable 2 × 2 reconstructed surface [31] is compared with that of a fully passivated nonreconstructed surface [The (111) surface Brillouin zone of the InAs and calculated band structures in a wide energy range are shown in Appendix C, Fig. 8.] Additional states emerge in the band structure of the reconstructed surface, which are not present in the band structure of the unreconstructed surface. Based on the projected contributions of the top four atomic layers (shown in red), the additional state is indeed a surface state. Figure 3(c) shows side and top views (inset) of the square modulus of the wave function in different atomic locations corresponding to the surface state band at the Γ point. The probability density of this state as a function of the depth shows that this state is highly localized near the reconstructed surface of the slab and decays faster to its bulk, further supporting the assignment of this band to a surface state due to the 2 × 2 reconstruction. We notice that this state is primarily localized around the three As atoms surrounding the In vacancy in the 2 × 2 reconstruction (inset) which establishes their origin from mostly As atomic orbitals, predominantly of *p*-orbital character. In Fig. 3(d) the calculated LDOS of the top four atomic layers is compared with the STS. Because of the limited thickness of the slab model, the DFT calculation does not capture the band bending, and hence the subband states are not captured either. Therefore the Fermi energy was shifted manually by 0.28 eV to compensate the band bending and to align the calculations with the experimentally observed STS data. The DFT results are in excellent agreement with the experiment with respect to the characteristic ∼0.1 eV spacing between the two main surface states as shown in Fig. 3(d). Note that the quantum size effect of the thin slab structure in the simulation is attributed to the quantized valence and conduction bands shown in Fig. 3(a), which should not be compared with the subbands we showed before just below the Fermi energy.

C. Response of the subband and surface states to crystal defects

So far, we have described the electronic properties of pristine InAs(111)A-(2 × 2) reconstructed surfaces. In this section, we shall demonstrate an interesting interplay between the subband and surface states in terms of their relative susceptibility when they encounter crystal defects. We have carried out spectroscopy measurements along a line, which encounters a single-atom dip vacancy island and three step edges, each one atom high. In Fig. 4(a) we show a STM

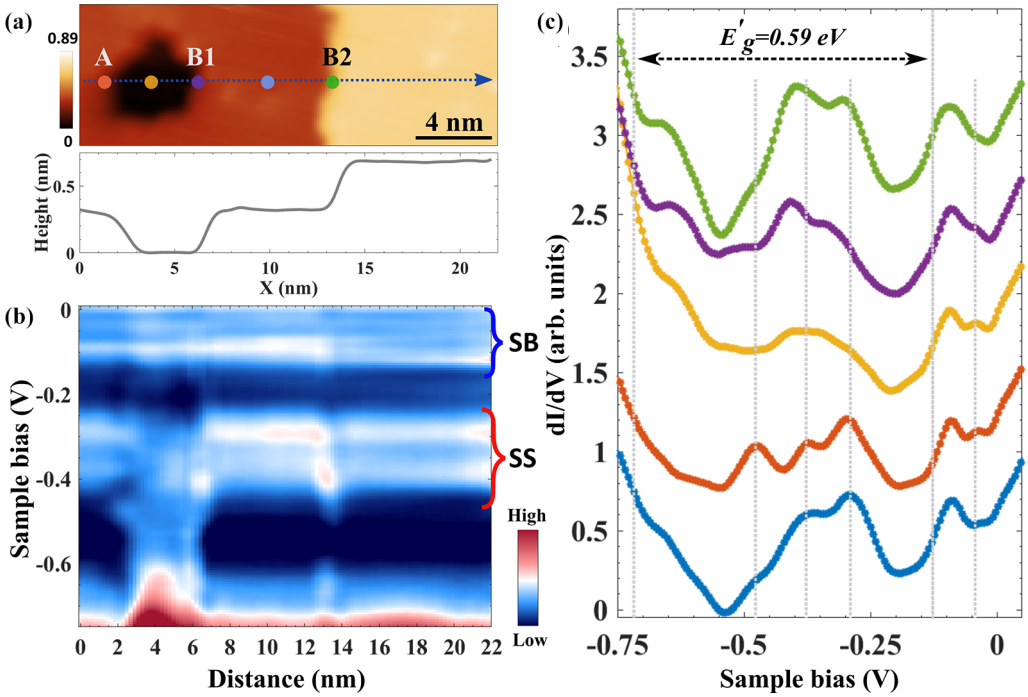

FIG. 4. Susceptibility of the confined bulk and the surface states. (a) An STM topographic image ($V_g = 1.5$ V, $I_T = 100$ pA) showing a single-atomic-depth vacancy island and the single-atomic-height step edges along with a height profile along the dotted arrow. (b) The measured dI/dV in terms of line spectra as a function of sample bias voltage and position. (c) Averaged dI/dV spectra [from (b) with a constant offset] in different positions on the surface marked by the corresponding colored dots in (a).

topography of such an area on the surface and plot the height profile taken along the dotted arrow. The lateral extension of the vacancy island is about 4 nm. Figure 4(b) shows dI/dV spectra, acquired along the line marked by the gray dotted arrow in Fig. 4(a), as a function of sample bias voltage and position (in the color map). Like the point spectra data, this line spectrum resolves once again the subband states (at energies $E_{C1} = -0.126$ eV and $E_{C2} = -0.48$ eV) and the surface states in the confined bulk gap (at the energies -0.29, -0.38, and -0.47 eV) below the Fermi energy. However, in these measurements the two surface states at the energies -0.29 and -0.38 eV are resolved very sharply by the tip along with the lowest subband states. The data acquired on both sides of the vacancy island show an overall confined band gap of about 0.59 eV (very close to the aforementioned value) below the Fermi energy, further confirming the downward band bending. In Fig. 4(b), the subband states appear as a bright line at just below the Fermi energy and above the confined band gap on the surface, as seen before. Before reaching the vacancy island, until around the position 2 nm, both the surface states and subband states remain unperturbed. Within the vacancy island, the surface states are significantly modified and lose their individual identity, and they further retain their features again after crossing it [Fig. 4(b)]. Within the vacancy island the surface states are perturbed. In contrast, the energy position of the subband states remains nearly unperturbed under the vacancy island defect and on the three step edges along the line. In Fig. 4(c), we show a quantitative comparison of the spectral features by averaging dI/dV spectra at different sample locations along the line of measurements on various crystal defects, namely, the vacancy island and three step edges. The color of the spectra represents the average dI/dV measured at the specific places marked by the dots in Fig. 4(a). On the vacancy island (yellow curve), all the surface states are rounded out into a broader mixed state, losing their energy position identities compared with the clean-region ones (blue curve) and those on the step edges (orange, purple, and green curves). For the case of the step edges, we found a notable contrast in spectra between step edge A (orange curve) and step edges B1 and B2 (purple and green curves). While the surface state positions near -0.28 and -0.37 eV for step edges B1 and B2 shift to a lower energy, the surface states of step edge A remain unchanged compared with the surface state positions of the clean region (blue curve). This is possibly a result of the similarity in crystallographic angle and orientation of steps B1 and B2 in comparison to step A, which has more of a broken, off-angle structure, seeming to be formed of the intersection between two crystallographic planes (e.g., see Appendix D). This contrast in the shifting surface state energy positions suggests that steps B1 and B2 act as charged defects [1], while step A is more likely to be electrostatically neutral [35].

Interestingly, we notice from Figs. 4(b) and 4(c) that the subband states remain resilient in their energy positions for both kinds of defects, unlike surface states. Similar robustness of these subband states was previously probed in different hybrid Al islands on InAs nanowire [36]. This apparent contrast in the susceptibility between the subband and surface states arises from their interactions with the defect potentials imposed by the crystal defects on the surface. Since the crystal defects are located exactly on the surface, the effective

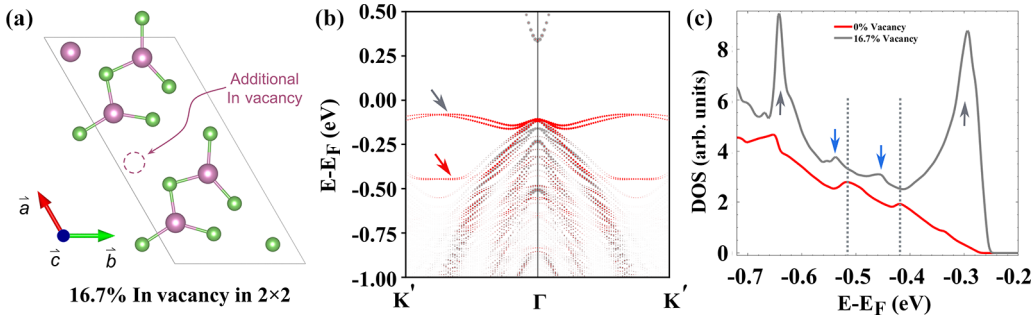

FIG. 5. Vacancy defects and position of surface states. (a) Additional indium vacancy in the 2 × 2 surface unit cell. (b) Calculated band structure of a 2 × 2 reconstructed InAs(111)A surface with 16.7% In vacancies. (c) A comparison of calculated electronic DOSs between the 2 × 2 reconstructed surface and with 16.7% In vacancy. This indicates that surface states shift to lower energy as a consequence of the vacancy defects.

interaction of an electronic states with this potential depends on how closely this state is localized to the surface. Being tightly bound to the surface, the surface states [Fig. 3(c)] interact strongly with the defect potential when compared with the subband states which exist significantly below the surface on the order of ∼10 nm [12,36]. At this length scale, these potentials get fully screened, and these confined states remain unperturbed against the crystal defects [35]. Screening of these defect potentials due to subband electrons on the surface leads to interesting consequences; for example, Friedel oscillation stemming from this screening has been shown to influence the structural ordering of the adatoms on the surface [37,38].

We notice that the energy positions of the surface states within the confined band gap vary from location to location on the sample. For instance, the surface state energies measured on comparatively clean areas from two different locations as shown in Figs. 2(b) and 4(c) (blue curve) show an energy difference of about 0.05 eV. We believe that this apparent difference originates from the local doping by the crystal imperfections present on the surface [1]. This phenomenon can be verified using DFT simulation results by comparing the energy positions of the surface states obtained from the 2 × 2 reconstructed surface and the surface with induced crystal imperfections in it. As an example, we introduce extra indium-vacancy crystal defects in the 2 × 2 surface unit cell shown in Fig. 5(a), and the resulting band structure is displayed in Fig. 5(b). We notice that the dispersion of the surface state bands has a significant amount of spin-orbit splitting. Figure 5(c) shows a comparison of the calculated electronic DOSs between the 2 × 2 reconstructed surface and the surface with 16.7% vacancy in it. Here we see that the energy positions of the surface states (marked by blue arrows) shift lower in the valence band. The amount of the shift and its direction can alter depending on the type of crystal imperfections, where the local chemical character of the electronic orbitals are different. This indicates that the substantial number of randomly distributed local surface defects collectively act similarly to a chemical dopant that modifies the local surface electronic spectrum [10]. We note that the large peaks in the DOS marked by gray arrows (Van Hove singularities) arise from dispersions along the Γ-$\bar{M}$ direction shown in Appendix E, Fig. 10 [39,40].

IV. CONCLUSION

We spectroscopically visualize the subband and surface states and show their relative susceptibility against crystal defects using low-temperature scanning tunneling microscopy and spectroscopy techniques on InAs(111)A-(2 × 2) reconstructed surfaces. The energy positions of the subband states are consistent with the results of empirical TB simulations, leading to our estimation of the confined bulk band gap at the surface and conduction band offset of 0.58 and 0.31 eV, respectively.

Combining the experimental results with first-principles DFT simulations, we explicitly uncover that the origin of the surface states in the confined band gap is from surface reconstruction and discuss their local structure. Moreover, we find that on an In-terminated surface, these surface states are attributed mostly to As atoms. We further investigate the susceptibility of the surface and subband states in the presence of different crystal defects and demonstrate that the surface states are strongly susceptible to the defect potential when

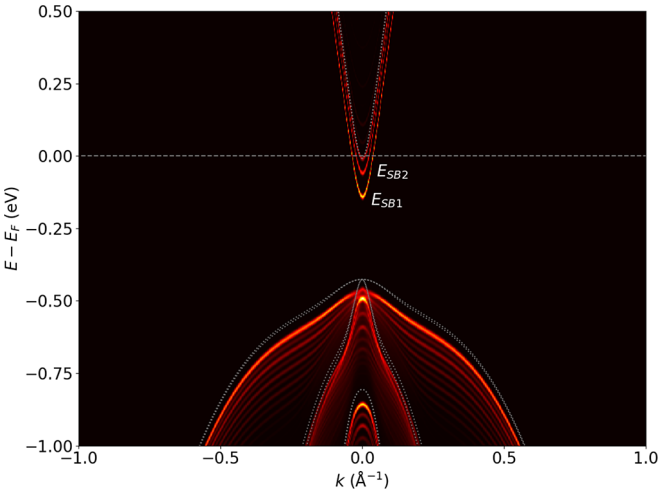

FIG. 6. Calculated band structure along the K' direction for the TB slab model of the surface with long-range band bending. The lowest two 2D subbands visible below the conduction band edge are labeled. The dotted lines show the bulk band structure of the primitive unit cell, shifted to align with the flat bands at the back of the slab.

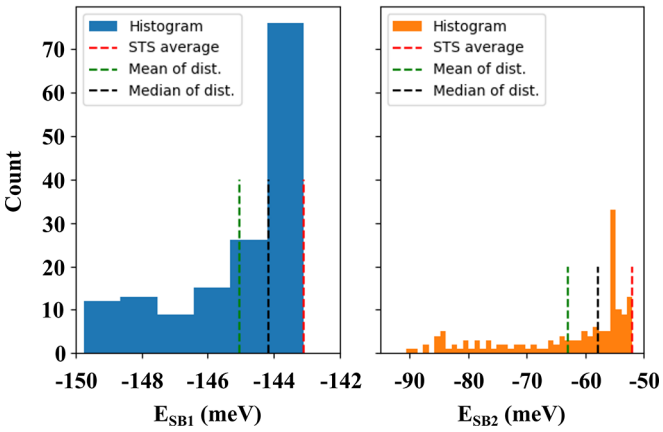

FIG. 7. Distribution of values for subband energy extraction of single-point spectra in a histogram plot with 1-meV bins. Note the different energy ranges. The median of the distribution (dist.) represents the data better than the mean value. The subband energy positions extracted from an average of all STS spectra (red dashed line) seems to represent the data well, although it is slightly shifted towards higher energies.

compared with the subband states. This apparent contrast follows from the length scale of the depth at which these subband and surface states exist and actively interact with the defect potentials on or near the surface.

ACKNOWLEDGMENTS

We gratefully acknowledge discussions with Kasper Grove-Rasmussen, Jan Gukelberger, and Sergej Schuwalow and support from Microsoft Quantum. Work at CMU was funded by the National Science Foundation (NSF) through Grant No. OISE-1743717. This research used resources of the National Energy Research Scientific Computing Center (NERSC), a DOE Office of Science User Facility supported by the Office of Science of the U.S. Department of Energy under Contract No. DE-AC02-05CH11231.

APPENDIX A: VISUALIZATION OF TB SUBBANDS

Figure 6 shows the band structure calculated for the TB model. We use a similar unfolding along Z onto the bulk Brillouin zone to that described for the DFT calculations in Appendix C.

APPENDIX B: SUBBAND ENERGY STATISTICS

Figure 7 shows a close-up of the extracted subband energy histograms for a set of spatially distributed spectra in clean areas of the sample.

APPENDIX C: DFT CALCULATIONS

In Fig. 8(a), the (111) surface Brillouin zone of the InAs structure is shown with the $\bar{K}$ high-symmetry point in the surface Brillouin zone that projects onto the bulk Γ-K path at K'. A large energy window of the unfolded band structures from the 2×2 In-vacancy reconstructed and unreconstructed surfaces is shown in Figs. 8(b) and 8(c), respectively. The observed quantized conduction band and the split-off band quantization are artifacts stemming from the finite size of the slab model. For both the reconstructed and unreconstructed surfaces, 30 atomic layers were used.

APPENDIX D: STEP EDGES

In order to make the step edge directions more visible, a topographic image of the area where the line spectra from Fig. 4(c) have been recorded was subjected to two-dimensional fast Fourier transform filtering, for enhanced atomic row contrast. Additionally, we took the two-dimensional derivative to make the step edges stand out. The results are shown in Fig. 9. From our knowledge of the

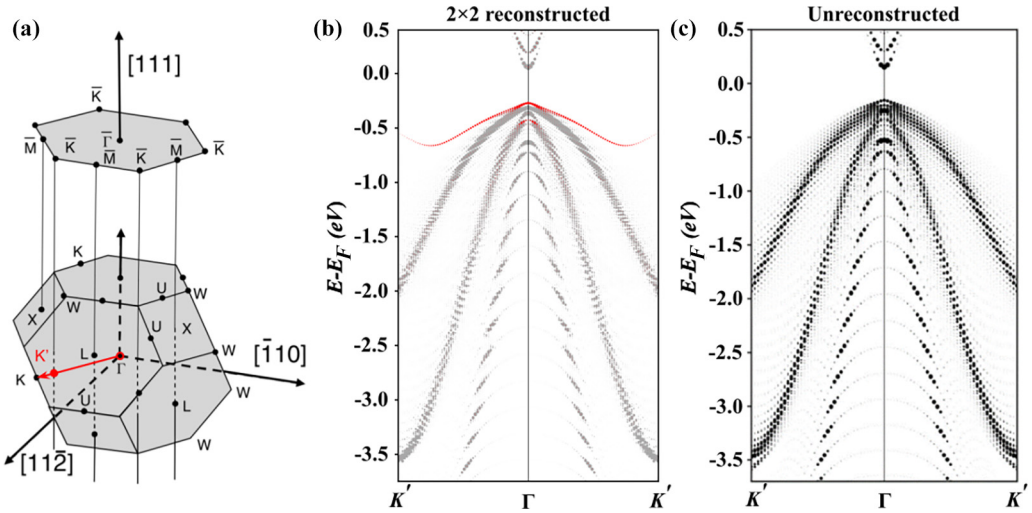

FIG. 8. (a) Visualization of the (111) surface Brillouin zone of the InAs structure showing where the $\bar{K}$ high-symmetry point in the surface Brillouin zone projects onto the bulk Γ-K path at K'. (b) and (c) Calculated band structure of a 2×2 reconstructed (b) and unreconstructed (c) InAs(111)A surface unfolded onto the primitive bulk Brillouin zone. The contributions of the top four atomic layers of the surface reconstruction are colored in red.

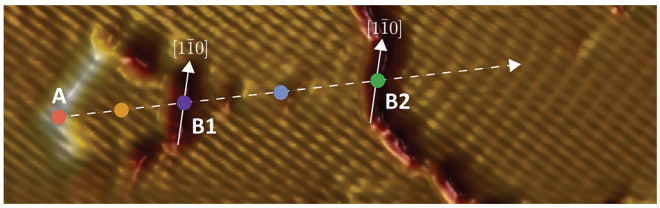

FIG. 9. Enhanced STM topographic image of the 2×2 reconstructed InAs(111)A surface in the region where the line spectra have been measured (along the dashed arrow). The positions of the spectra described in Fig. 4(c) are shown as colored dots. This figure reveals the crystallographic orientations of step edges A, B1, and B2.

sample mounting orientation and the recovered 2×2 surface reconstruction, the crystal direction along the step edges could be inferred to be [1$\bar{1}$0] along step edges B1 and B2 (shown by two arrows), and at position A, two crystal directions meet.

APPENDIX E: ORIGIN OF VAN HOVE SINGULARITIES

Figure 10 shows the 3D bands from the density of states calculation shown in Fig. 5(c). The Van Hove singularities arise from the flat region of the band shown with the dashed red line.

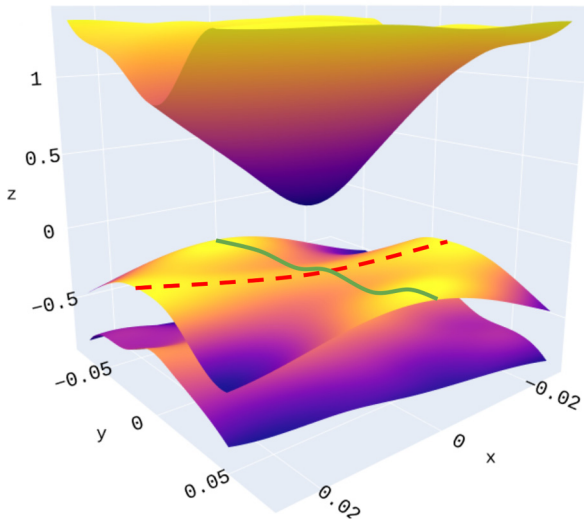

FIG. 10. 3D bands corresponding to the Van Hove singularities (sharp peaks) seen in the density of states. The dashed red line is along the Γ-$\bar{M}$ path, and the solid green line is along the Γ-$\bar{K}$ path shown in the main text.

[1] R. M. Feenstra, Tunneling spectroscopy of the (110) surface of direct-gap III-V semiconductors, Phys. Rev. B **50**, 4561 (1994).

[2] C. Thomas, A. T. Hatke, A. Tuaz, R. Kallaher, T. Wu, T. Wang, R. E. Diaz, G. C. Gardner, M. A. Capano, and M. J. Manfra, High-mobility InAs 2DEGs on GaSb substrates: A platform for mesoscopic quantum transport, Phys. Rev. Mater. **2**, 104602 (2018).

[3] J. Boos, W. Kruppa, B. Bennett, D. Park, S. Kirchoefer, R. Bass, and H. Dietrich, AlSb/InAs HEMT's for low-voltage, high-speed applications, IEEE Trans. Electron Devices **45**, 1869 (1998).

[4] A. Daničić, J. Radovanović, D. Indjin, and Z. Ikonić, Modeling of electron relaxation processes and the optical gain in a magnetic-field assisted THz quantum cascade laser, Phys. Scr. **2012**, 014017 (2012).

[5] D. Liang and X. P. Gao, Strong tuning of Rashba spin–orbit interaction in single InAs nanowires, Nano Lett. **12**, 3263 (2012).

[6] R. M. Lutchyn, J. D. Sau, and S. Das Sarma, Majorana Fermions and a Topological Phase Transition in Semiconductor-Superconductor Heterostructures, Phys. Rev. Lett. **105**, 077001 (2010).

[7] Y. Oreg, G. Refael, and F. von Oppen, Helical Liquids and Majorana Bound States in Quantum Wires, Phys. Rev. Lett. **105**, 177002 (2010).

[8] K. Kanisawa, M. J. Butcher, H. Yamaguchi, and Y. Hirayama, Imaging of Friedel Oscillation Patterns of Two-Dimensionally Accumulated Electrons at Epitaxially Grown InAs(111)A Surfaces, Phys. Rev. Lett. **86**, 3384 (2001).

[9] S. Fölsch, J. Yang, C. Nacci, and K. Kanisawa, Atom-By-Atom Quantum State Control in Adatom Chains on a Semiconductor, Phys. Rev. Lett. **103**, 096104 (2009).

[10] K. Kanisawa and T. Fujisawa, Mechanism of electron accumulation layer formation at the MBE-grown InAs(111)A surface, Hyomen Kagaku **29**, 747 (2008).

[11] K. Kanisawa, Correlation between adatom dynamics and electron accumulation at the epitaxial InAs(111)A surface, J. Cryst. Growth **378**, 8 (2013).

[12] M. Noguchi, K. Hirakawa, and T. Ikoma, Intrinsic Electron Accumulation Layers on Reconstructed Clean InAs (100) Surfaces, Phys. Rev. Lett. **66**, 2243 (1991).

[13] S. Schuwalow, N. B. M. Schröter, J. Gukelberger, C. Thomas, V. Strocov, J. Gamble, A. Chikina, M. Caputo, J. Krieger, G. C. Gardner, M. Troyer, G. Aeppli, M. J. Manfra, and P. Krogstrup, Band structure extraction at hybrid narrow-gap semiconductor-metal interfaces, Adv. Sci. **8**, 2003087 (2021).

[14] S. Yang, N. B. M. Schröter, V. N. Strocov, S. Schuwalow, M. Rajpalk, K. Ohtani, P. Krogstrup, G. W. Winkler, J. Gukelberger, D. Gresch, G. Aeppli, R. M. Lutchyn, and N. Marom, Electronic structure of InAs and InSb surfaces: Density functional theory and angle-resolved photoemission spectroscopy, Adv. Quantum Technol. **5**, 2100033 (2022).

[15] S. Smidstrup, T. Markussen, P. Vancraeyveld, J. Wellendorff, J. Schneider, T. Gunst, B. Verstichel, D. Stradi, P. A. Khomyakov, U. G. Vej-Hansen, M.-E. Lee, S. T. Chill, F. Rasmussen, G. Penazzi, F. Corsetti, A. Ojanperä, K. Jensen, M. L. N. Palsgaard, U. Martinez, A. Blom *et al.*, QuantumATK: An integrated platform of electronic and atomic-scale modelling tools, J. Phys.: Condens. Matter **32**, 015901 (2020).

[16] J.-M. Jancu, R. Scholz, F. Beltram, and F. Bassani, Empirical spds* tight-binding calculation for cubic semiconductors: General method and material parameters, Phys. Rev. B **57**, 6493 (1998).

[17] I. Vurgaftman, J. R. Meyer, and L. R. Ram-Mohan, Band parameters for III-V compound semiconductors and their alloys, J. Appl. Phys. **89**, 5815 (2001).

[18] G. Kresse, and D. Joubert, From ultrasoft pseudopotentials to the projector augmented-wave method, Phys. Rev. B **59**, 1758 (1999).

[19] G. Kresse and J. Furthmüller, Efficient iterative schemes for *ab initio* total-energy calculations using a plane-wave basis set, Phys. Rev. B **54**, 11169 (1996).

[20] G. Kresse and J. Furthmüller, Efficiency of ab-initio total energy calculations for metals and semiconductors using a plane-wave basis set, Comput. Mater. Sci. **6**, 15 (1996).

[21] G. Kresse and J. Hafner, *Ab initio* molecular dynamics for open-shell transition metals, Phys. Rev. B **48**, 13115 (1993).

[22] G. Kresse and J. Hafner, *Ab initio* molecular-dynamics simulation of the liquid-metal–amorphous-semiconductor transition in germanium, Phys. Rev. B **49**, 14251 (1994).

[23] P. E. Blöchl, Projector augmented-wave method, Phys. Rev. B **50**, 17953 (1994).

[24] J. P. Perdew, K. Burke, and M. Ernzerhof, Generalized Gradient Approximation Made Simple, Phys. Rev. Lett. **77**, 3865 (1996).

[25] S. L. Dudarev, G. A. Botton, S. Y. Savrasov, C. J. Humphreys, and A. P. Sutton, Electron-energy-loss spectra and the structural stability of nickel oxide: An LSDA+U study, Phys. Rev. B **57**, 1505 (1998).

[26] M. Yu, S. Yang, C. Wu, and N. Marom, Machine learning the Hubbard U parameter in DFT+U using Bayesian optimization, npj Comput. Mater. **6**, 180 (2020).

[27] S. Yang, D. Dardzinski, A. Hwang, D. I. Pikulin, G. W. Winkler, and N. Marom, First-principles feasibility assessment of a topological insulator at the InAs/GaSb interface, Phys. Rev. Mater. **5**, 084204 (2021).

[28] M. Yu, S. Moayedpour, S. Yang, D. Dardzinski, C. Wu, V. S. Pribiag, and N. Marom, Dependence of the electronic structure of the EuS/InAs interface on the bonding configuration, Phys. Rev. Mater. **5**, 064606 (2021).

[29] D. Dardzinski, M. Yu, S. Moayedpour, and N. Marom, Best practices for first-principles simulations of epitaxial inorganic interfaces, J. Phys.: Condens. Matter **34**, 233002 (2022).

[30] J. Bohr, R. Feidenhans, M. Nielsen, M. Toney, R. L. Johnson, and I. K. Robinson, Model-Independent Structure Determination of the InSb(111)2× 2 Surface with Use of Synchrotron X-Ray Diffraction, Phys. Rev. Lett. **54**, 1275 (1985).

[31] A. Taguchi and K. Kanisawa, Stable reconstruction and adsorbates of InAs(111)A surface, Appl. Surf. Sci. **252**, 5263 (2006).

[32] S. Zelzer, R. Batabyal, D. Dardzinski, N. Marom, K. Grove-Rasmussen, and P. Krogstrup, Scale-dependent optimized homoepitaxy of InAs(111)A, Cryst. Growth Des. **22**, 5958 (2022).

[33] Zero bias in STM sets the E_F, and our TB model calculation estimates its position to be 11 meV below the bulk CBM.

[34] Y. Niimi, K. Kanisawa, H. Kojima, H. Kambara, Y. Hirayama, S. Tarucha, and H. Fukuyama, STM/STS measurements of two-dimensional electronic states in magnetic fields at epitaxially grown InAs(111)A surfaces, J. Phys.: Conf. Ser. **61**, 874 (2007).

[35] A. P. Romagosa, S. Zelzer, R. Batabyal, and P. Krogstrup, Estimation of electrostatic screened potential at a stepedge on InAs(111)A (unpublished).

[36] J. Reiner, A. K. Nayak, A. Tulchinsky, A. Steinbok, T. Koren, N. Morali, R. Batabyal, J.-H. Kang, N. Avraham, Y. Oreg, H. Shtrikman, and H. Beidenkopf, Spectroscopic Visualization of a Robust Electronic Response of Semiconducting Nanowires to Deposition of Superconducting Islands, Phys. Rev. X **10**, 011002 (2020).

[37] M. Ono, Y. Nishigata, T. Nishio, T. Eguchi, and Y. Hasegawa, Electrostatic Potential Screened by a Two-Dimensional Electron System: A Real-Space Observation by Scanning-Tunneling Spectroscopy, Phys. Rev. Lett. **96**, 016801 (2006).

[38] B. Kiraly, E. J. Knol, K. Volckaert, D. Biswas, A. N. Rudenko, D. A. Prishchenko, V. G. Mazurenko, M. I. Katsnelson, P. Hofmann, D. Wegner, and A. A. Khajetoorians, Anisotropic Two-Dimensional Screening at the Surface of Black Phosphorus, Phys. Rev. Lett. **123**, 216403 (2019).

[39] L. Van Hove, The occurrence of singularities in the elastic frequency distribution of a crystal, Phys. Rev. **89**, 1189 (1953).

[40] M. Y. Toriyama, A. M. Ganose, M. Dylla, S. Anand, J. Park, M. K. Brod, J. M. Munro, K. A. Persson, A. Jain, and G. J. Snyder, How to analyse a density of states, Mater. Today Electron. **1**, 100002 (2022).